

# Ring Origami: Snap-Folding of Rings with Different Geometries

Shuai Wu, Liang Yue, Yi Jin, Xiaohao Sun, Cole Zemelka, H. Jerry Qi,\*  
and Ruike Zhao\*

Origami folding and thin structure buckling are intensively studied for structural transformations with large packing ratio for various biomedical, robotic, and aerospace applications. The folding of circular rings has shown bistable snap-through deformation under simple twisting motion and demonstrates a large area change to 11% of its undeformed configuration. Motivated by the large area change and the self-guided deformation through snap-folding, it is intended to design ring origami assemblies with unprecedented packing ratios. Herein, through finite-element analysis, snap-folding behaviors of single ring with different geometries (circular, elliptical, rounded rectangular, and rounded triangular shapes) are studied for ring origami assemblies for functional foldable structures. Geometric parameters' effects on the foldability, stability, and the packing ratio are investigated and are validated experimentally. With different rings as basic building blocks, the folding of ring origami assemblies including linear-patterned rounded rectangular rings, radial-patterned elliptical rings, and 3D crossing circular rings is further experimentally demonstrated, which show significant packing ratios of 7% and 2.5% of the initial areas, and 0.3% of the initial volume, respectively. It is envisioned that the reported snap-folding of origami rings will provide alternative strategies to design foldable/deployable structures and devices with reliable self-guided deformation and large area change.

## 1. Introduction


The development of foldable and reconfigurable structures is attracting increasing interests in various engineering fields. The folding/deploying processes enable complex functional shape morphing and tunable physical properties for robotic motions,<sup>[1]</sup> flexible electronic devices,<sup>[2]</sup> active metamaterials,<sup>[3]</sup> and deployable structures.<sup>[4]</sup> Meanwhile, the transformations can permit effective packing of structures for applications such as satellite solar panels<sup>[5]</sup> and biomedical stents<sup>[6]</sup> which have limited payload storage space before functioning. Efforts have been devoted to various morphing mechanisms to achieve desired shape changing and structure packing. Origami, from the art of paper folding, is one folding strategy that realizes transformations between 2D materials and 3D structures with good compactness.<sup>[7]</sup> However, most origami systems rely on controlled and continuously applied external driving force to achieve preferred shape transformation. The precision of the deformed shape is completely deter-

mined by the accuracy of the external force and boundary conditions, which hinders the reliability and error tolerance of the folding/deploying process.<sup>[8]</sup> An alternative folding strategy adopts buckling deformations of slim beams or thin shells with a bistable/multistable feature. In this case, once the external load reaches a critical value, the structures trigger a snap-through deformation to desired stable configurations with locally minimized energy in a self-guided manner. The snapping behavior leads to the deformed state with high geometric precision and a high tolerance of loading error under external perturbations. This strategy has been adopted in designs such as metamaterials for multistable shape reconfiguration and energy absorption,<sup>[9]</sup> folding/deploying of 2D and 3D lattice structures<sup>[10]</sup> and spherical shells,<sup>[11]</sup> and surface instabilities of artificial tissues.<sup>[12]</sup>

Rationally designed ring-shaped structures demonstrate bistable foldable behaviors utilizing the snap-through mechanism under simple twisting or bending, showing the merits of significant area reduction.<sup>[13]</sup> For example, the folding of a circular ring shows a large area change to 11% of its undeformed configuration. Motivated by the large area change

S. Wu, Y. Jin, C. Zemelka, R. Zhao  
Department of Mechanical and Aerospace Engineering  
The Ohio State University  
Columbus, OH 43210, USA  
E-mail: zhao.2885@osu.edu

L. Yue, X. Sun, H. J. Qi  
The George W. Woodruff School of Mechanical Engineering  
Georgia Institute of Technology  
Atlanta, GA 30332, USA  
E-mail: qih@me.gatech.edu

 The ORCID identification number(s) for the author(s) of this article can be found under <https://doi.org/10.1002/aisy.202100107>.

© 2021 The Authors. Advanced Intelligent Systems published by Wiley-VCH GmbH. This is an open access article under the terms of the Creative Commons Attribution License, which permits use, distribution and reproduction in any medium, provided the original work is properly cited.

DOI: 10.1002/aisy.202100107

and the self-guided deformation through snap-folding, we introduce a design strategy to achieve unprecedented packing ratios by ring origami assemblies consist of multiple rings, shown by the schematics in **Figure 1**. As shown in **Figure 1a**, six stiff rings with enveloped soft films are connected by hinges as building panels of a dome-shaped structure. By stacking the rings together, the structure transforms into a 2D configuration with a reduced volume (**Figure 1b**). Then the snap-folding of stacked rings (**Figure 1c**) leads to a stable folded configuration with a significantly reduced area and volume (**Figure 1d**). Note that, the highly packed structure is able to deploy to the initial configuration, and the entire folding and deploying process is reversible. To utilize this snap-folding strategy for tremendous packing ratio, it is important to understand the controlling parameters of folding for single rings with specific geometries. Existing works only study the folding of circular rings.<sup>[13,14]</sup> However, circular rings are inefficient when it comes to ring assemblies in a close-packed manner. The exploration of other foldable ring geometries that can be better assembled to close-packed large structures is desired. In this work, starting from circular rings, we study the snap-folding of different rings with more complex geometries (elliptical, rounded rectangular, and rounded triangular rings), which provides more flexibility and versatility in designing 2D and 3D assemblies. For each type of ring, the influence of ring geometries on the foldability, stability, and packing ratio are parametrically investigated via finite-element analysis (FEA). The results from FEA are validated by experimentally folding plastic rings with different geometries. With different rings as basic building units, we later experimentally demonstrate the folding of ring origami assemblies including linear-patterned rounded rectangle rings, radial-patterned elliptical rings, and 3D crossing circular rings, which show significant area changes.

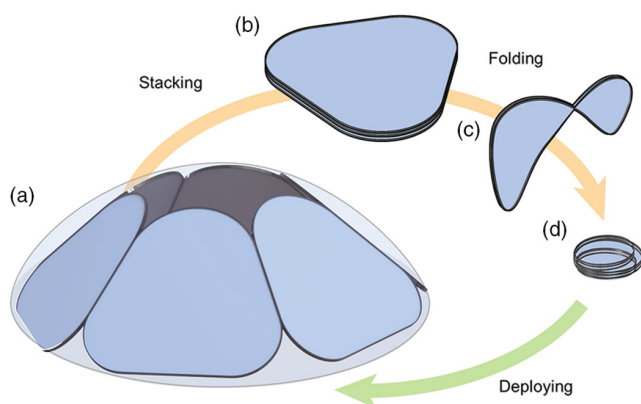


**Figure 1.** Schematics of ring origami assembly with the capability of large area/volume change via reversible folding and deploying. a) A dome-like structure assembled by multiple rings with enveloped soft films. b) A 2D structure by stacking all rings in (a). c) Snap-folding process of the stacked rings. d) Folded rings at a stable state with a further reduced area. The folded structure can be deployed to the initial configuration.

## 2. Results

### 2.1. Snap-Folding of Circular Rings

We start from twisting a circular ring (**Figure 2**) to gain initial insights into the snap-folding process. As shown in **Figure 2a**, the circular ring has a radius of  $R$  and a rectangle cross-section with the thickness of  $t$  and the height of  $h$ . Here, in FEA, the ring buckling is induced by applying twisting loads with opposite directions to two ends of the circular ring along the  $x$  axis, with a final twisting angle of  $\theta = \pi$ . During the folding process, the twisted ends rotate while being free to translate along  $x$  axis, and the corresponding reaction moment  $M$  is recorded in terms of the twisting angle. To capture the snap-through instability during the buckling of the ring-shaped objects, a displacement control method is used in all FEA throughout the work. Note that although applying bending can also realize the ring buckling deformation along an alternative loading path (**Figure S1**, Supporting Information), we focus on snap-folding of rings via twisting in this work as twisting is more robust in terms of folding different ring geometries. We first study the influence of cross-sectional geometry on the circular ring's foldability and stability by varying the cross-sectional geometry ( $h/t = 1, 1.5, 2,$  and  $4$ ) while fixing the ring's overall size ( $R/t = 200$ ). **Figure 2b** shows the normalized moment ( $MR/EJ$ ) versus twisting angle ( $\theta$ ) curves (moment-angle curves) and corresponding ring configurations after twisting, where  $E$  is Young's modulus of the material and  $J$  is the torsion constant determined by the cross-sectional geometry. In this article, we study rings with cross-sectional dimensions  $h$  and  $t$  much smaller than the span of rings. In general, increasing cross-sectional aspect ratio  $h/t$  would increase the circular ring's foldability and stability (**Figure 2b**). For the ring with a square cross-section ( $h/t = 1$ , orange curve), the moment first increases and then slightly decreases before further going up, indicating an unfoldable ring. A similar trend is observed for the case with  $h/t = 1.5$  (purple curve) during the folding process, and the purple circle at  $\theta = \pi$  corresponds to the configuration of the unfoldable ring. For cross sections with  $h/t = 2$  and  $4$ , after reaching the snapping point, the moment rapidly decreases toward zero, which indicates both circular rings are foldable. The whole folding process of the rings is a buckling behavior, whose evolution during twisting load highly depends on the ring's bending and torsional rigidities and thus the cross-sectional aspect ratio  $h/t$ . A foldable ring requires bending-dominated deformation with the preferred in-plane bending (bending axis of the ring parallel to  $h$ ) and the bending stiffness proportional to  $Eht^3$ . Larger  $h/t$  promotes the preferred bending due to the low bending stiffness in the preferred direction and thus leads to high foldability. On the contrary, smaller  $h/t$  prevents the preferred bending due to the relatively large bending stiffness in the preferred direction and results in poorer foldability. Through the snap-folding, a large circular ring can be folded into a configuration with three overlapped small circular rings that have only 11% of the initial area, realizing a tremendous packing ratio. Although both rings with  $h/t = 2$  and  $4$  are foldable, the stability of folding is determined by whether the moment drops to/below zero. Therefore,  $h/t = 2$  shows an unstable snap-folding and  $h/t = 4$  indicates a stable snap-folding. Note that in reality, the FEA-predicted

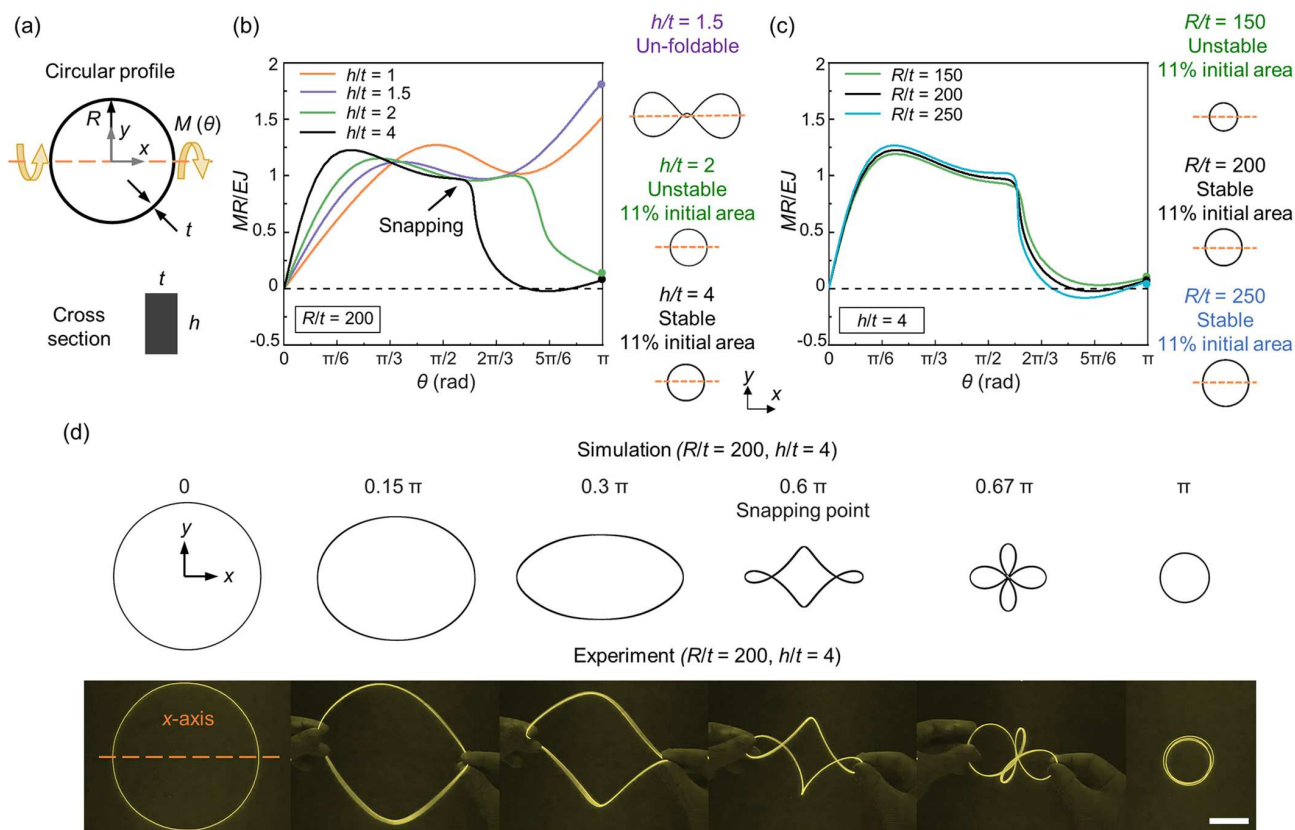


**Figure 2.** FEA simulation and experimental validation of the snap-folding of circular rings. a) Geometric parameters and loading conditions of circular rings. b, c) FEA results of normalized moment-twisting angle curves for rings with b) different cross-sectional geometries and c) different sizes. d) Comparison of FEA and experimental folding processes of a circular ring with stable folding. Scale bar: 5 cm.

unstable snap-folding with the lowest moment close to zero after snapping can still lead to stable folding due to the friction induced by surface contact of the ring during folding.

Next, we vary the circular ring radius ( $R/t = 150, 200$ , and  $250$ ) while fixing the cross-sectional geometry ( $h/t = 4$ ), as shown in Figure 2c. It can be observed that all cases are foldable and the moment-angle landscapes are similar, with only small shifts that change the stability of folded configurations. Increasing ring radius in general leads to a slightly higher normalized moment before snapping and a lower minimum moment after snapping, enabling folding that is more stable. Unstable folding for  $R/t = 150$  and stable folding for  $R/t = 200$  and  $250$  are obtained with the same folded configurations (11% of the initial area). To validate the FEA result, we pick a circular ring ( $R/t = 200, h/t = 4$ ) with stable folding, shown in Figure 2d. The top row shows the detailed snap-folding process corresponding to the black curve in Figure 2a,b. A plastic ring (Young's modulus 1.8 GPa) with the exact same geometry is cast (see Experimental Section and Figure S2, Supporting Information, for material fabrication and characterization), with its folding resulting in a reduced area to 11% of the initial value demonstrated by the bottom row of Figure 2d. The experiment shows very good agreement with the FEA prediction. Note that the FEA allows interpenetration, and the slight difference of final folded configurations from FEA and experiments is mainly due to the contact and the resultant friction during folding of rings

in experiments. The folding–deploying process demonstrates a reversible behavior and snapping is observed in both folding and deploying processes. From FEA, the maximum strain reaches the highest value of 0.4% near the two twisting ends when the ring is about to snap. Note that, the ring material behaves elastically under at least 2% of tensile strain (Figure S2, Supporting Information). Varying the cross-sectional geometry, an alternative ring ( $R/t = 200, h/t = 1$ ) is also fabricated to validate the FEA-predicted unfoldable behavior (Video S1, Supporting Information).

## 2.2. Snap-Folding of Elliptical Rings

We next investigate the snap-folding of elliptical rings, whose geometry has reduced symmetry compared with circular rings (Figure 3). As shown in Figure 3a, the elliptical ring has the semiminor axis along  $x$  axis with length of  $b$ , the semimajor axis along  $y$  axis with length of  $a$ , and a rectangle cross section with height of  $h$  and thickness of  $t$ . The snap-folding is studied when a twisting load with an angle of  $\theta$  is applied either along  $x$  axis (dashed orange lines) or  $y$  axis (dashed blue lines). The reaction moment  $M$  is recorded in terms of the twisting angle  $\theta$ . We first vary the cross-sectional aspect ratio ( $h/t = 1, 1.5, 2, 4$ ) while fixing the ring's profile ( $b/a = 0.5$ ) and size ( $a/t = 200$ ). Figure 3b shows the plots of normalized moment ( $Ma/EJ$ ) versus twisting angle ( $\theta$  around  $x$  axis) for different cross-sectional aspect ratios and

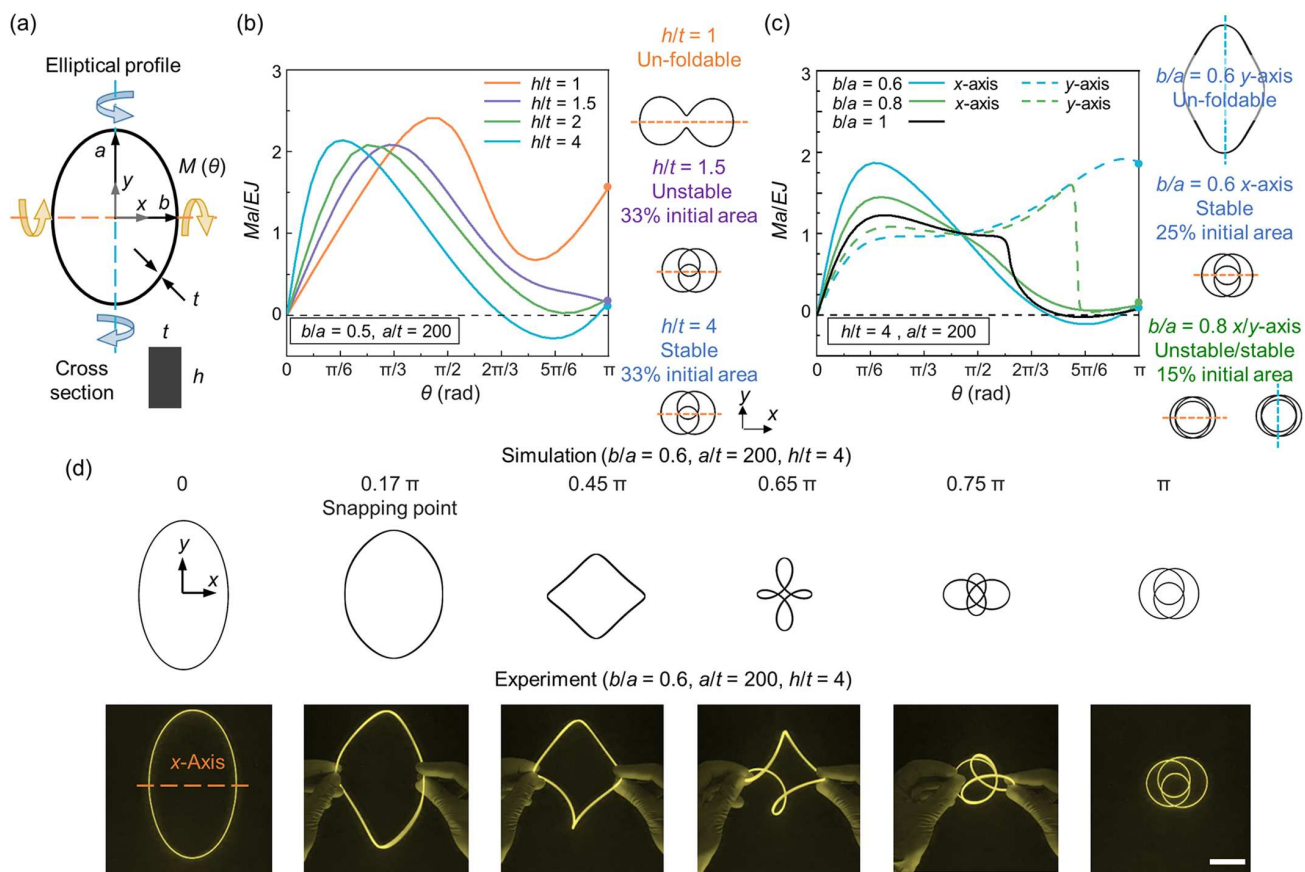


**Figure 3.** FEA simulation and experimental validation of the snap-folding of elliptical rings. a) Geometric parameters and loading conditions of elliptical rings. b,c) FEA results of normalized moment–twisting angle curves for rings with b) different cross-sectional geometries and c) different elliptical profile aspect ratios and twisting axes. d) Comparison of FEA and experimental folding processes of an elliptical ring with stable folding. Scale bar: 5 cm.

their corresponding final configurations at  $\theta = \pi$ . Under the assumption of  $h, t \ll a$ , increasing  $h/t$  from 1 to 4 leads to increased foldability and stability, and earlier snapping points ( $\theta = 0.47\pi, 0.32\pi, 0.25\pi$ , and  $0.17\pi$  for  $h/t = 1, 1.5, 2, 4$ , respectively). As shown by the final configurations in Figure 3b, the elliptical ring is un-foldable for  $h/t = 1$ , foldable but unstable for  $h/t = 1.5$ , and foldable and stable for  $h/t = 2, 4$ . For foldable elliptical rings, the final folded configurations (33% of the initial area) are not affected by  $h/t$ .

Figure 3c shows how the elliptical profile aspect ratio ( $b/a$ ) and the twisting axis ( $x$  axis or  $y$  axis) affect foldability and stability of the snap-folding when the cross-sectional geometry is fixed at  $h/t = 4$ . Here the semimajor axis  $a$  is fixed at  $a/t = 200$  and the semiminor axis  $b$  is varied to adjust the elliptical shape ( $b/a = 0.6, 0.8$ , and  $1$ ). Increasing  $b/a$  value from  $0.6$  to  $1$ , the elliptical profile gradually returns to a circular ring with a stable folding, denoted by the solid black curve in Figure 3c. When the elliptical ring with  $b/a = 0.6$  is twisted along the  $y$  axis (dashed blue curve), the overall increasing moment indicates an un-foldable behavior (top configuration in Figure 3c). However, by switching the twisting axis to  $x$  axis, the elliptical ring with  $b/a = 0.6$  shows a stable folding behavior (solid blue curve) with the area of the folded configuration to be 25% of the initial value, shown by the middle configuration in

Figure 3c. It is interesting to observe that regardless the twisting axis, the maximum moment during folding is roughly the same for the same  $b/a$ , whereas the snapping point is much earlier when twisting along the ring's minor axis ( $x$  axis). For the elliptical ring of  $b/a = 0.8$ , it indicates foldable behavior with the same final configuration (15% of the initial area) regardless the twisting axis. As the moment at the final state is close to zero but above, the folding behavior is at the intersection of being unstable/stable. As discussed previously, friction could facilitate a stable folding in the experiment. It can be observed that with an increasing  $b/a$  ratio =  $0.5, 0.6, 0.8$ , and  $1$ , the elliptical rings reveal an improved packing ratio (33%, 25%, 15%, and 11% with respect to the initial area). To validate the FEA result, a plastic elliptical ring ( $b/a = 0.6, a/t = 200, h/t = 4$ ) is cast, as shown in Figure 3d. The top row shows the detailed stable snap-folding process predicted by FEA, with a reduced area to 25% of the initial value. The bottom row shows the experimental snap-folding process, indicating very good agreement with the FEA. The folding–deploying process demonstrates a reversible behavior and snapping is observed in both folding and deploying processes. An un-foldable behavior of an elliptical ring with  $b/a = 0.6, a/t = 200, h/t = 1$  is also experimentally tested to validate the FEA prediction (Video S2, Supporting Information).



### 2.3. Snap-Folding of Rounded Rectangular Rings

In this section, we investigate the snap-folding of rectangular rings with rounded corners. As shown in **Figure 4a**, the rounded rectangular ring has long edges with a length of  $2a$ , short edges with a length of  $2b$ , a rectangle cross-section with a height of  $h$  and a thickness of  $t$ , and rounded corners with a radius of  $r$ . The

snap-folding is studied when a twisting load with an angle of  $\theta$  is applied either along  $x$  axis (dashed orange lines) or  $y$  axis (dashed blue lines). The reaction moment  $M$  is recorded in terms of the twisting angle  $\theta$ . We first vary the cross-sectional aspect ratio ( $h/t = 1, 1.5, 2$ , and  $4$ ) while fixing the ring's profile ( $b/a = 0.5$ ,  $r/a = 0.3$ ), size ( $a/t = 200$ ). **Figure 4b** shows the plots of normalized moment ( $Ma/EJ$ ) versus twisting angle ( $\theta$  around  $x$  axis) for

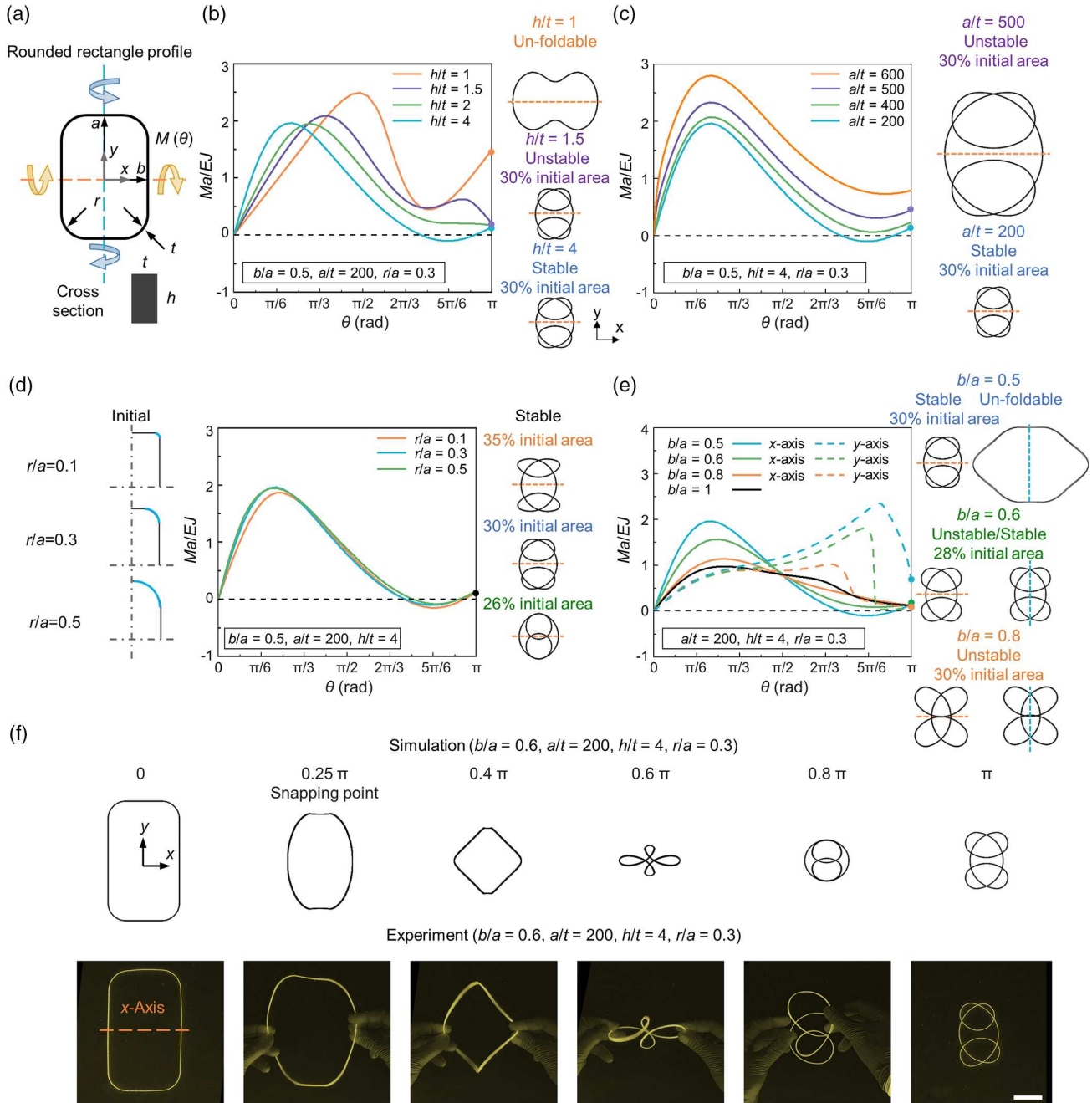


**Figure 4.** FEA simulation and experimental validation of the snap-folding of rounded rectangular rings. a) Geometric parameters and loading conditions of rounded rectangular rings. b–e) FEA results of normalized moment–twisting angle curves for rings with b) different cross-sectional geometries; c) different sizes; d) different rounded corners; e) different rounded rectangular profile aspect ratios and twisting axes. f) Comparison of FEA and experimental folding processes of a rounded rectangular ring with stable folding. Scale bar: 5 cm.

different cross-sectional aspect ratios and their corresponding final configurations at  $\theta = \pi$ . Similar to circular rings and elliptical rings, a larger  $h/t$  increases the foldability and stability of folding: the ring is unfoldable for  $h/t = 1$ , foldable but unstable for  $h/t = 1.5, 2$ , and foldable and stable for  $h/t = 4$ . As shown by the middle and bottom configurations in Figure 4b, as long as the ring is foldable, the configurations of folded rings (30% of the initial area) are not affected by  $h/t$ . Next, we study the influence of ring size  $a/t$  on snap-folding of the ring while fixing other dimensions ( $b/a = 0.5$ ,  $r/a = 0.3$ ,  $h/t = 4$ ) and twisting axis ( $x$  axis), as shown in Figure 4c. It can be observed that all rings ( $a/t = 200, 400, 500$ , and  $600$ ) are foldable with the same folded configurations (30% of the initial area). For different ring sizes, although a same snapping point ( $\theta = 0.22\pi$ ) is obtained, the stability of folding is largely affected (stable for  $a/t = 200$ , unstable for  $a/t = 400, 500, 600$ ). Figure 4d shows how the rounded corner affects the snap-folding while fixing the overall size of the rounded rectangle ( $a/t = 200$ ,  $b/a = 0.5$ ). Three rectangle profiles are shown by the quarter models with varied corner radius ( $r/a = 0.1, 0.3$ , and  $0.5$  denoted by the blue color). From moment-angle curves, increasing the  $r/a$  value does not influence the ring's foldability and stability. However, the stable folded configurations at  $\theta = \pi$  are very different due to the distinct shapes at the ring corners. A higher  $r/a$  value (0.1, 0.3, and 0.5) leads to a better packing ratio (35%, 30%, and 26% to the initial area, respectively).

Figure 4e shows how the rectangular aspect ratio ( $b/a$ ) and the twisting axis ( $x$  axis or  $y$  axis) affect foldability and stability of the snap-folding while fixing the cross-sectional geometry and corner radius ( $h/t = 4$ ,  $r/a = 0.3$ ). The rectangle length is fixed at  $a/t = 200$  and the rectangle width is varied to adjust the rectangle shape ( $b/a = 0.5, 0.6, 0.8$ , and  $1$ ). When increasing  $b/a$  value from 0.5 to 1, the rounded rectangle profile gradually returns to a rounded square ring with a foldable but unstable folding behavior denoted by the solid black curve in Figure 4e (see Figure S3, Supporting Information, for more results about the rounded square ring folding). When the rounded rectangle with  $b/a = 0.5$  is twisted along the  $y$  axis (dashed blue curve), the overall increasing moment indicates an unfoldable behavior (top right configuration). However, by switching the twisting axis to  $x$  axis, the ring with  $b/a = 0.5$  shows a stable folding behavior (solid blue curve) with the area reducing to 30% of the initial value at folded state  $\theta = \pi$ . The maximum moment during folding is roughly the same for the same  $b/a$  regardless the twisting axis, while the snapping point is much earlier when twisting along  $x$  axis. For the rectangular ring of  $b/a = 0.6$ , foldable behavior is obtained with the same final configuration (28% of the initial area) regardless the twisting axis. Though the solid/dashed green moment-angle curves are right above zero, meaning that the folding behavior is at the intersection of being unstable/stable, experimentally the friction may lead to a stable folding. When increasing  $b/a$  value to 0.8, the moment-angle curves further approach the square ring, resulting in an unstable folding (30% of the initial area at folded configuration) regardless the twisting axis. To validate the FEA result, a plastic ring ( $b/a = 0.6$ ,  $a/t = 200$ ,  $h/t = 4$ ,  $r/a = 0.3$ ) is molded, as shown in Figure 4f. The top row shows the detailed stable snap-folding process predicted by FEA, with a reduced area to 28% of the initial value. The bottom row shows

the experimental snap-folding process, indicating very good agreement with the FEA. The folding-deploying process demonstrates a reversible behavior and snapping is observed in both folding and deploying processes. An FEA-predicted unfoldable behavior of a rounded rectangular ring with  $b/a = 0.6$ ,  $a/t = 200$ ,  $h/t = 1$ ,  $r/a = 0.3$  is also experimentally validated (Video S3, Supporting Information).

#### 2.4. Snap-Folding of Rounded Triangular Rings

Triangle is one efficient geometry to build close-packed 2D/3D structures. In this section, we investigate the snap-folding of isosceles triangular rings with rounded corners. As shown in Figure 5a, the rounded triangular ring has the base with length of  $a$ , the vertex angle of  $\alpha$ , a rectangle cross section with height of  $h$  and thickness of  $t$ , and rounded corners with radius of  $r$ . Twisting loads with opposite directions are applied to two ends of the axis of symmetry ( $y$  axis, dashed blue line) of the rounded triangular ring, with a final twisting angle of  $\theta = \pi$ . The reaction moment  $M$  is recorded in terms of the twisting angle  $\theta$ . We first vary the vertex angle  $\alpha = 30^\circ, 60^\circ, 90^\circ$ , and  $120^\circ$  while fixing the rounded triangular ring's base ( $a/t = 600$ ), corner radius ( $r/a = 1/30$ ), and cross-sectional shape ( $h/t = 4$ ), as shown in Figure 5b. The normalized moment ( $Ma/EJ$ ) versus twisting angle ( $\theta$  around  $y$  axis) are evaluated. A larger vertex angle leads to a higher normalized moment at the same snapping point ( $\theta = 0.09\pi$ ) and in the meantime increases the foldability and stability. For the acute triangle with  $\alpha = 30^\circ$  and  $60^\circ$ , the moment has an overall increasing trend during folding, indicating un-foldable behaviors (top deformation configuration in Figure 5b). By changing the corner radius and cross-section geometry, the equilateral triangular ring can be foldable (Figure S4, Supporting Information). For the isosceles right triangular ring ( $\alpha = 90^\circ$ ), the moment decreases toward but above zero after snapping, revealing an unstable folding (bottom left configuration). For the obtuse triangular ring with  $\alpha = 120^\circ$ , the ring shows a stable folding behavior (bottom right configuration).

As shown in Figure 5c, we next vary the cross-sectional aspect ratio ( $h/t = 1, 1.5, 2, 4$ ) of the rounded triangular rings while fixing their vertex angle, size, and corner radius ( $\alpha = 120^\circ$ ,  $a/t = 600$ ,  $r/a = 1/15$ ). The moment-twisting angle plots depict the increased foldability and stability, together with an earlier snapping point when increasing  $h/t$ . The results indicate unfoldable behaviors for  $h/t = 1$  and  $1.5$ , unstable folding for  $h/t = 2$ , and stable folding for  $h/t = 4$ , with their deformed configurations shown to the right of the plots. Figure 5d shows how the corner radius affects the snap-folding of the triangular rings. A set of radii ( $r/a = 1/10, 1/15, 1/20$ , and  $1/30$ ) are investigated. From moment-angle curves, increasing  $r/a$  has negligible effect on the rings' foldability and stability, but the folded configurations at  $\theta = \pi$  are very different due to the distinct corner shapes of the undeformed rings. From Figure 5e, with the fixed triangular profile ( $\alpha = 120^\circ$ ,  $r/a = 1/30$ ) and cross section ( $h/t = 4$ ), increasing ring sizes ( $a/t = 600, 800$ , and  $1000$ ) does not affect the folding behavior and the folded configuration. This demonstrates good scalability of the triangular ring with reliable folding. To validate the FEA result, a plastic rounded triangular ring ( $\alpha = 120^\circ$ ,

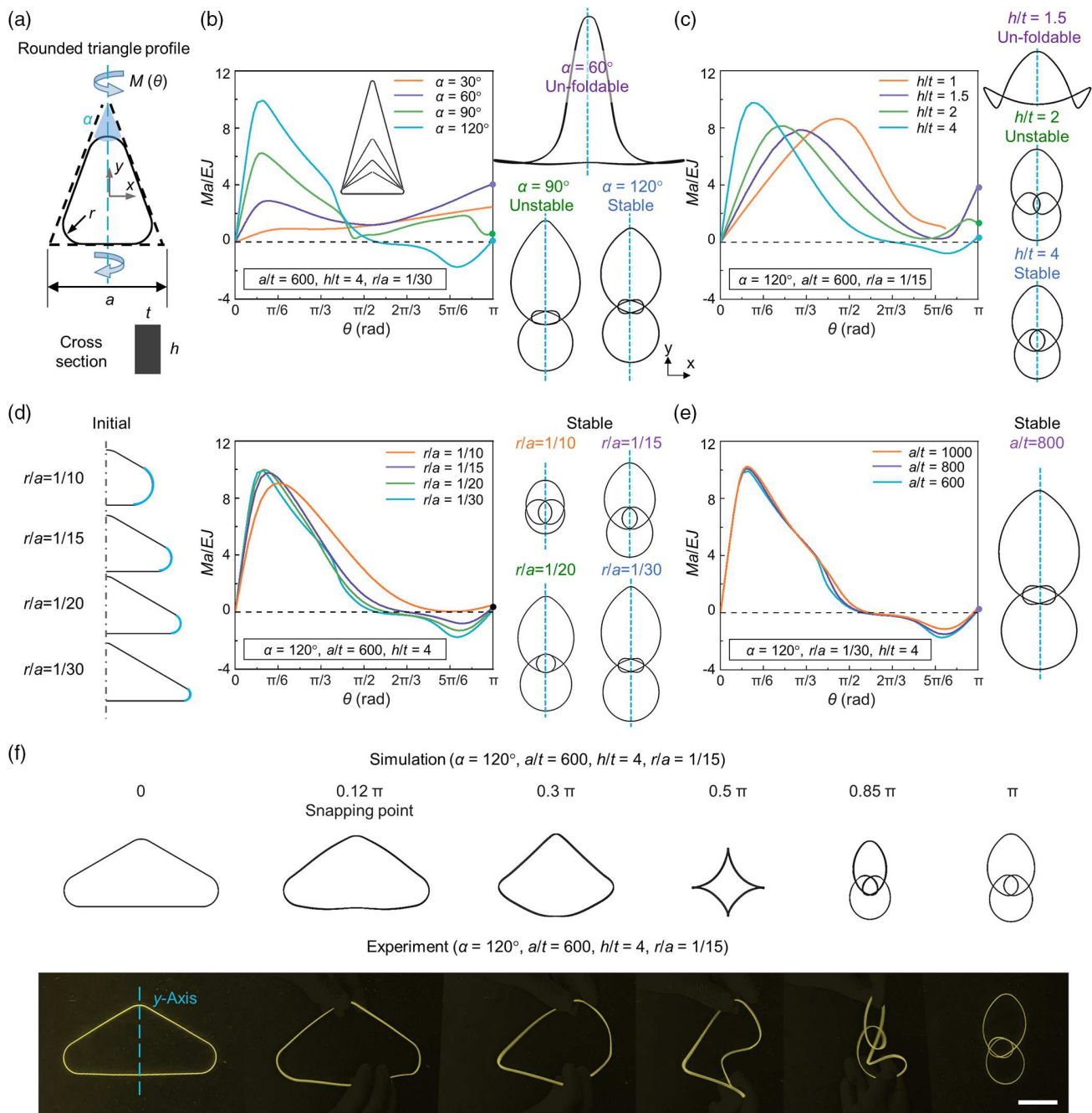


**Figure 5.** FEA simulation and experimental validation of the snap-folding of rounded triangular rings. a) Geometric parameters and loading conditions of the rounded triangular ring. b–e) FEA results of normalized moment–twisting angle curves for rings with b) different vertex angles; c) different cross-sectional geometries; d) different rounded corners; e) different sizes. f) Comparison of FEA and experimental folding processes of a rounded triangular ring with stable folding. Scale bar: 5 cm.

$a/t = 600, h/t = 4, r/a = 1/15$ ) is cast, as shown in Figure 5f. The top row shows the detailed stable snap-folding process predicted by FEA. The bottom row shows the experimental snap-folding process, showing decent agreement with the FEA prediction. The experimental configurations during folding are slightly different from simulations due to the uncontrollable

snapping process. The folding–deploying process demonstrates a reversible behavior and snapping is observed in both folding and deploying processes. An FEA-predicted unfoldable behavior of a rounded triangular ring with  $\alpha = 120^\circ, a/t = 600, h/t = 1, r/a = 1/15$  is also experimentally validated (Video S4, Supporting Information).



### 3. Ring Origami Assemblies with Outstanding Packing Capabilities

The single rings with optimized stable-foldable geometries serve as building blocks for ring origami assemblies for largely enhanced packing performance. Guided by the rationally designed foldable rings, we demonstrate two examples of 2D ring origami assemblies based on rounded rectangular rings and elliptical rings and one 3D ring sphere based on crossing circular rings. As shown in **Figure 6a**, the rounded rectangles ( $b/a = 0.6$ ,

$a/t = 200$ ,  $h/t = 4$ ,  $r/a = 0.3$ ) in **Figure 4f** are assembled into a two-by-two linear pattern. Adjacent rectangle edges are connected by tape hinges, which constrain the relative translational motion of the two connected edges while allowing their relative rotation. A reduced area to only 7% of the initial state is achieved at the ultimate folded configuration after the stacking and folding steps. As shown in **Figure 6b**, the two-by-two assembly is first folded into overlapped rings along its two structural centerlines, reducing the total area to one-fourth. The overlapped rings are then twisted around the short axis of the rectangle, folding into

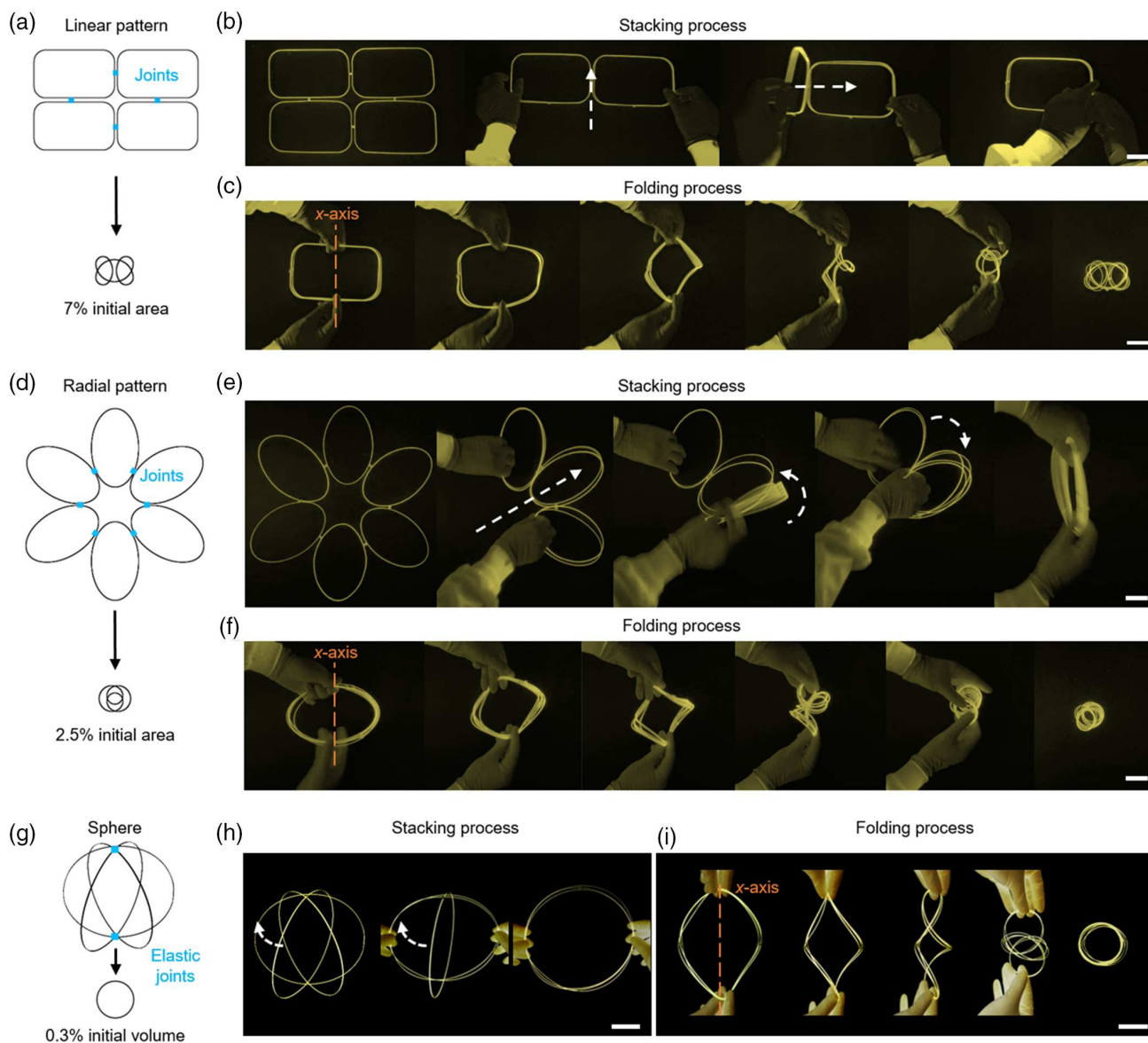


**Figure 6.** Experimental folding process of ring origami assemblies with large packing ratio. a) Assembly schematic of the two-by-two linear pattern of rounded rectangular rings and its stable folded configuration with a reduced area to 7% of the initial value. b) Experimental images of the stacking process and c) folding process of the linear pattern. d) Assembly schematic of the radial pattern of six elliptical rings and its stable folded configuration with a reduced area to 2.5% of the initial value. Experimental images of the e) stacking process and f) folding process of the radial pattern. g) Assembly schematic of a 3D ring sphere using three crossing circular rings connected by cylindrical silicone rubber joints and its stable folded configuration with a reduced volume to 0.3% of the initial value. Experimental images of the h) stacking process and i) folding process of the sphere assembly. Scale bar: 5 cm.



a stable configuration with a tremendously reduced area (Figure 6c). The folding process is reversible and the folded structure can be deployed back to the initial assembly (Video S5, Supporting Information). Note that during deployment, the first step of snap-deploying of the folded overlapped rings also shows self-guided deformation, whereas the further deployment of the rings to the original linear pattern would require mechanical assistance. Based on the same concept, six elliptical rings ( $b/a = 0.6$ ,  $a/t = 200$ ,  $h/t = 4$ ) in Figure 3d are assembled into a 2D radial pattern, as shown in Figure 6d. The same two-step folding strategy can be utilized to achieve excellent packing ratio (2.5% area of the initial assembly). As shown in Figure 6e, the assembly is first stacked into six overlapped elliptical rings, followed by a twisting-induced snap-folding to the ultimate stable-folded configuration (Figure 6f). Similarly, the structure can go through reversible folding and deploying with proper manipulation (Video S5, Supporting Information). With rationally designed joints, the deploying process can be more automatic. To illustrate this, a 3D ring sphere is made of three crossing circular rings connected by cylindrical silicone rubber as joints (Figure S5, Supporting Information), as shown in Figure 6g. The three circular rings have a relative angle of  $120^\circ$  and can be stacked together into an in-plane multiring structure (Figure 6h). During this procedure, elastic energy is stored in the joints. The stacked rings can then be folded to a stable state under twisting loads (Figure 6i), reducing the entire volume of the structure to only 0.3% of the initial sphere. With the help of the designed elastic joints, the structure can deploy from its folded state in only 2.4 s by releasing the stored elastic energy (Video S6, Supporting Information).

#### 4. Conclusions

In this work, snap-folding of different rings (circular, elliptical, rounded rectangular, and rounded triangular rings) under twisting are investigated for large area changes and high packing ratios. Parametric studies are carried out for each type of the ring to optimize the snap-folding process for the self-guided deformation with a stable folded configuration. With rationally designed single rings, high packing ratios are achieved with significantly reduced area (11%, 15%, and 26% of initial area for specific circular, elliptical, and rounded-rectangle rings). The optimized designs of the stable-foldable rectangular rings and elliptical rings are further assembled into large 2D structures and stable-foldable circular rings are assembled into a 3D structure for tremendously enhanced packing ratios (7%, 2.5% of initial area, and 0.3% of initial volume, respectively). The reported snap-folding of ring origami with different geometries provides a new strategy to design foldable structures with high-precision self-guided stable folding and a high tolerance of loading error under external perturbations. We envision this concept will enable applications for shape morphing and foldable/deployable structures with outstanding and reliable packing and deploying capabilities. In this work, the ring systems without film are investigated to provide general insight into the snap-folding concept and how it can contribute to high-precision foldable structures and devices. Although attaching a soft film to the stiff ring would

not largely affect its overall folding behavior, the systematic study is still of interest to future study.

#### 5. Experimental Section

**Finite-Element Analysis:** The snap-folding processes of circular, elliptical, rounded rectangular, and rounded triangular rings were simulated using the commercial software ABAQUS 2018 (Dassault Systèmes, France). Linear elastic model was adopted for all rings with Young's modulus of 1.8 GPa and Poisson's ratio of 0.3 (see Figure S6, Supporting Information, for influence of Poisson's ratio on snap-folding). C3D8R element was used for all simulations. The ring buckling was induced by applying twisting loads with opposite directions to two ends of the rings along x-axis or y-axis, with a final twisting angle of  $\pi$ . During the folding process, the twisted ends rotated while being free to translate along the twisting axis, and the corresponding reaction moment was recorded in terms of the twisting angle. A small damping factor of  $10^{-10}$  was used to stabilize the ring buckling simulations with a negligible amount of dissipated energy (Figure S7, Supporting Information). To focus on the influence of ring geometry and dimension on the snap-folding process, the self-contact of the ring was not considered in this work, instead of limiting the ring origami concept to a specific material system with specific surface properties.

**Fabrication of the Ring Origami:** All rings in the experiments were cast by specially synthesized polymer resin. The UV curable resin contained isobornyl acrylate (Sigma Aldrich, USA) and tricyclodecanedimethanol diacrylate (Sigma Aldrich) with the weight ratio of 80:20. In addition, 1 wt% photoinitiator (Irgacure 819, Sigma Aldrich) was added for free radical polymerization and 0.01 wt% fluorescent dye (Solvent green 5, Oricem International Ltd., China) was added for light fluorescence. All rings with different geometries were prepared by filling the predesigned polydimethylsiloxane molds (PDMS) (Sylgard 184, DowCorning Inc., USA) with the well-mixed resin, followed by curing under UV light for one minute and a post curing in the oven for 10 min at  $80^\circ\text{C}$ . A Young's modulus of 1.8 GPa was measured for the cured resin with a good linear elastic behavior under cyclic loadings (Figure S2, Supporting Information). See supporting information for the details of mechanical characterizations.

#### Acknowledgements

S.W., L.Y., and Y.J. contributed equally to this work. R.Z., S.W., Y.J., C.Z. acknowledge NSF Award EFMA-2029643 and NSF Career Award CMMI-1943070. H.J.Q., L.Y., X.S. acknowledge the support of NSF Award EFMA-2029157 and AFOSR grant (FA9550-20-1-0306; Dr. B.-L. "Les" Lee, Program Manager). *The Interactive Supporting Information of this article can be found at:* <https://authorea.com/doi/full/10.22541/au.162255786.68312076/v2>

#### Conflict of Interest

The authors declare no conflict of interest.

#### Data Availability Statement

Data available on request from the authors.

#### Keywords

bistability, buckling instabilities, foldable structures, origami

Received: May 31, 2021

Revised: July 7, 2021

Published online:

- [1] a) W. Kim, J. Byun, J.-K. Kim, W.-Y. Choi, K. Jakobsen, J. Jakobsen, D.-Y. Lee, K.-J. Cho, *Sci. Robot.* **2019**, 4; b) S. Li, J. J. Stampfli, H. J. Xu, E. Malkin, E. V. Diaz, D. Rus, R. J. Wood, presented at 2019 Int. Conf. on Robotics and Automation (ICRA), May 20–24, **2019**; c) R. V. Martinez, C. R. Fish, X. Chen, G. M. Whitesides, *Adv. Funct. Mater.* **2012**, 22, 1376; d) S. Li, D. M. Vogt, D. Rus, R. J. Wood, *Proc. Natl Acad. Sci.* **2017**, 114, 13132.
- [2] a) Q. Cheng, Z. Song, T. Ma, B. B. Smith, R. Tang, H. Yu, H. Jiang, C. K. Chan, *Nano Lett.* **2013**, 13, 4969; b) L. S. Novelino, Q. Ze, S. Wu, G. H. Paulino, R. Zhao, *Proc. Natl Acad. Sci.* **2020**, 117, 24096; c) S. A. Nauroze, L. S. Novelino, M. M. Tentzeris, G. H. Paulino, *Proc. Natl Acad. Sci.* **2018**, 115, 13210; d) Q. Ze, X. Kuang, S. Wu, J. Wong, S. M. Montgomery, R. Zhang, J. M. Kovitz, F. Yang, H. J. Qi, R. Zhao, *Adv. Mater.* **2020**, 32, 1906657.
- [3] S. M. Montgomery, S. Wu, X. Kuang, C. D. Armstrong, C. Zemelka, Q. Ze, R. Zhang, R. Zhao, H. J. Qi, *Adv. Funct. Mater.* **2021**, 31, 2005319.
- [4] D. Melancon, B. Gorissen, C. J. García-Mora, C. Hoberman, K. Bertoldi, *Nature* **2021**, 592, 545.
- [5] a) S. A. Zirbel, R. J. Lang, M. W. Thomson, D. A. Sigel, P. E. Walkemeyer, B. P. Trease, S. P. Magleby, L. L. Howell, *J. Mech. Design* **2013**, 135; b) T. Chen, O. R. Bilal, R. Lang, C. Daraio, K. Shea, *Phys. Rev. Appl.* **2019**, 11, 064069.
- [6] K. Kuribayashi, K. Tsuchiya, Z. You, D. Tomus, M. Umemoto, T. Ito, M. Sasaki, *Mater. Sci. Eng. A* **2006**, 419, 131.
- [7] a) S. J. Callens, A. A. Zadpoor, *Mater. Today* **2018**, 21, 241; b) Y. Chen, R. Peng, Z. You, *Science* **2015**, 349, 396.
- [8] a) A. Kotikian, C. McMahan, E. C. Davidson, J. M. Muhammad, R. D. Weeks, C. Daraio, J. A. Lewis, *Sci. Robot.* **2019**, 4; b) Z. Fang, H. Song, Y. Zhang, B. Jin, J. Wu, Q. Zhao, T. Xie, *Matter* **2020**, 2, 1187; c) J. H. Na, A. A. Evans, J. Bae, M. C. Chiappelli, C. D. Santangelo, R. J. Lang, T. C. Hull, R. C. Hayward, *Adv. Mater.* **2015**, 27, 79; d) Y. Mao, K. Yu, M. S. Isakov, J. Wu, M. L. Dunn, H. J. Qi, *Sci. Rep.* **2015**, 5, 1.
- [9] a) A. Rafsanjani, A. Akbarzadeh, D. Pasini, *Adv. Mater.* **2015**, 27, 5931; b) S. Shan, S. H. Kang, J. R. Raney, P. Wang, L. Fang, F. Candido, J. A. Lewis, K. Bertoldi, *Adv. Mater.* **2015**, 27, 4296.
- [10] a) B. Haghpanah, L. Salari-Sharif, P. Pourrajab, J. Hopkins, L. Valdevit, *Adv. Mater.* **2016**, 28, 7915; b) A. Nasto, A. Ajdari, A. Lazarus, A. Vaziri, P. M. Reis, *Soft Matter* **2013**, 9, 6796; c) N. P. Bende, A. A. Evans, S. Innes-Gold, L. A. Marin, I. Cohen, R. C. Hayward, C. D. Santangelo, *Proc. Natl. Acad. Sci.* **2015**, 112, 11175.
- [11] J. Shim, C. Perdigou, E. R. Chen, K. Bertoldi, P. M. Reis, *Proc. Natl. Acad. Sci.* **2012**, 109, 5978.
- [12] a) R. Zhao, T. Zhang, M. Diab, H. Gao, K.-S. Kim, *Extreme Mech. Lett.* **2015**, 4, 76; b) R. Zhao, X. Zhao, *J. Appl. Mech.* **2017**, 84.
- [13] G. Yoshiaki, W. Yasuhito, K. Toshihiro, O. Makoto, *Int. J. Solids Struct.* **1992**, 29, 893.
- [14] a) P. Pai, A. Palazotto, *Int. J. Solids Struct.* **1996**, 33, 1335; b) P.-O. Mouthuy, M. Coulombier, T. Pardoën, J.-P. Raskin, A. M. Jonas, *Nat. Commun.* **2012**, 3, 1; c) J. Bae, J.-H. Na, C. D. Santangelo, R. C. Hayward, *Polymer* **2014**, 55, 5908.